Chemical Engineering Journal 531 (2026) 173902

Contents lists available at ScienceDirect

Chemical Engineering Journal

journal homepage: www.elsevier.com/locate/cej

Unveiling the temperature-dependent reaction dynamics of Li_3BO_3: Formation and carbonation mechanisms via in situ synchrotron XRD

María José Orozco [a,b], María Laura Grasso [c], Pedro Alonso-Sánchez [d], Federico Cova [e], María Laura Rodriguez [a], María Valeria Blanco [f,*], Fabiana C. Gennari [b,c,**]

[a] Instituto de Investigación en Tecnología Química (INTEQUI-UNSL/CONICET), Almirante Brown 1450, 5700, San Luis, Argentina
[b] Universidad Nacional de Cuyo (Instituto Balseiro), Centro Atómico Bariloche (CNEA), Av. Bustillo 9500, R8402AGP, San Carlos de Bariloche, Río Negro, Argentina
[c] Departamento Fisicoquímica de Materiales, Gerencia de Investigación Aplicada, Centro Atómico Bariloche (CNEA), Av. Bustillo 9500, R8402AGP, San Carlos de Bariloche, Río Negro, Argentina
[d] Instituto de Nanociencia y Materiales de Aragón (CSIC-Universidad de Zaragoza), C/ Pedro Cerbuna 12, 50009, Zaragoza, Spain
[e] Sincrotrón ALBA, Carrer de la Llum 2-26, Cerdanyola del Vallés, 08290, Spain
[f] Instituto de Ciencia de Materiales de Barcelona, ICMAB-CSIC, Campus UAB, 08193, Bellaterra, Cataluña, Spain

ARTICLE INFO

Keywords:
Tri-lithium borate
Synthesis
CO_2 capture
Carbonation mechanism
X-ray diffraction

ABSTRACT

Tri-lithium borate (Li_3BO_3) has emerged as a promising CO_2 sorbent for intermediate-high temperature applications, particularly in post-combustion carbon capture processes. Its high CO_2 uptake capacity, along with improved kinetic performance when modified with additives, makes it a compelling alternative to conventional lithium-based sorbents. Upon carbonation, Li_3BO_3 reacts to form lithium carbonate (Li_2CO_3) and lithium borates, such as $Li_6B_4O_9$ and $LiBO_2$, with reaction kinetics strongly dependent on CO_2 partial pressure and temperature. However, the fundamental high-temperature reaction dynamics governing Li_3BO_3 formation and carbonation remain largely unexplored. This study employs time-resolved in situ synchrotron X-ray diffraction (XRD) to unveil the phase transformations and reaction pathway occurring during Li_3BO_3 synthesis and its reaction with CO_2. Structural evolution during the heating of a mechanically milled H_3BO_3-Li_2CO_3 mixture from room temperature to 600 °C reveals a successful transformation to Li_3BO_3 via a multi-step mechanism. In situ high-temperature synchrotron XRD measurements coupled with Rietveld refinement demonstrate that the carbonation mechanism of Li_3BO_3 is significantly influenced by CO_2 partial pressure. Under 10% of CO_2, $Li_6B_4O_9$ and Li_2CO_3 are identified from 400 °C, followed by the formation of $Li_{(2+x)}C_{(1-x)}B_xO_3$ solid solution between 530 °C and 580 °C. In contrast, under pure CO_2, $Li_6B_4O_9$ forms at 350 °C, with $LiBO_2$ appearing at higher temperatures. Notably, the temperature range of $Li_{(2+x)}C_{(1-x)}B_xO_3$ stabilization shifts toward higher temperatures under pure CO_2 conditions. Understanding these transformations is essential for optimizing the performance and stability of Li_3BO_3 in CO_2 capture applications and serves as a basis for future additive optimization, contributing to the broader development of high-temperature sorbent materials.

1. Introduction

Anthropogenic carbon dioxide (CO_2) emissions resulting from the combustion of fossil fuels and industrial processes constitute one of the principal contributors to the intensification of global climate change [1]. As concentrations of CO_2 in the atmosphere continue to rise, there is growing interest in developing effective carbon capture and storage (CCS) technologies capable of mitigating these emissions [2,3]. Among the various capture strategies, post-combustion CO_2 capture remains particularly relevant due to its applicability to existing power generation infrastructure, such as coal-fired and natural gas power plants, as well as industrial sectors including cement and steel manufacturing [4]. These sectors are responsible of flue gas emissions with different CO_2 concentrations depending on their source, with values between 3% and 8% by volume for natural gas power plants [5,6], while the highest concentration are associated with coal-fired power plants (10–18% in

* Corresponding author.
** Correspondence to: F. C. Gennari, Universidad Nacional de Cuyo (Instituto Balseiro), Centro Atómico Bariloche (CNEA), Av. Bustillo 9500, R8402AGP, San Carlos de Bariloche, Río Negro, Argentina.
E-mail addresses: vblanco2@icmab.es (M.V. Blanco), fabiana.gennari@ib.edu.ar (F.C. Gennari).

https://doi.org/10.1016/j.cej.2026.173902
Received 14 October 2025; Received in revised form 23 December 2025; Accepted 6 February 2026
Available online 17 February 2026
1385-8947/© 2026 The Authors. Published by Elsevier B.V. This is an open access article under the CC BY-NC-ND license (http://creativecommons.org/licenses/by-nc-nd/4.0/).

volume) [5,7]. Traditionally, chemical absorption using aqueous amine solvents has dominated commercial CCS implementations. However, this approach suffers from several limitations, including high energy requirements for solvent regeneration, chemical degradation, and operational issues related to corrosion and solvent loss [8]. In response to these constraints, considerable attention has shifted toward the development of solid-state sorbents [9], which offer advantages such as improved thermal stability, lower regeneration energy penalties, and potential integration with high-temperature industrial gas streams without extensive heat exchange infrastructure [10–13].

Within the category of high-temperature CO_2 sorbents, lithium-based ceramics have demonstrated promising performance characteristics. Materials such as lithium zirconate (Li_2ZrO_3, 500–700 °C), lithium orthosilicate (Li_4SiO_4, 500–700 °C), lithium aluminate (Li_5AlO_4, 500–750 °C), and lithium cuprate (Li_2CuO_2, 450–700 °C) have been widely studied for their ability to capture CO_2 at elevated temperatures [14–17]. These materials exhibit good theoretical CO_2 uptake capacities and selectivity, and are typically synthesized via simple solid-state synthesis methods [18–23], but their practical application is hindered by slow carbonation and decarbonation kinetics, high desorption temperatures, and structural degradation over repeated cycling. These shortcomings have motivated the search for alternative lithium-based compounds with improved performance under intermediate and high-temperature conditions [24–26].

Tri-lithium borate (Li_3BO_3) has recently gained recognition as a particularly promising sorbent, exhibiting a high gravimetric CO_2 uptake capacity of over 11 $mmol\,g^{-1}$, approximately 50 wt%, at 520 °C under pure CO_2 [27], positioning it among the most efficient lithium-based solid sorbents reported to date. In addition to its high capacity, Li_3BO_3 modified by additives displays excellent reversibility and relatively fast reaction kinetics during both carbonation and decarbonation cycles, making it an attractive candidate for post-combustion capture systems operating within the 500–650 °C temperature window [27–29]. In particular, Li_3BO_3-based sorbents modified with a low content of NaOH [29], are a highly attractive alternative for CO_2 capture in post-combustion processes when compared to other solid sorbents like CaO, Li_4SiO_4 and Li_2ZrO_3. Among the most competitive advantages of Li_3BO_3 based sorbents compared with CaO, Li_4SiO_4 and Li_2ZrO_3 are the high CO_2 capture capacity, reaching up to 36–37 wt% under low CO_2 concentrations; the low energy consumption for the capture process, as indicated by the lowest enthalpy of reaction values (120 ± 7 kJ/mol) and the high carbonation rate (37 wt% in 1000 s at 525 °C) [29]. Furthermore, Li_3BO_3 sorbent modified with 0.25 mol of NaOH maintains a high capture capacity of 36 wt% over 20 cycles at a moderate temperature of 525 °C under low concentration of CO_2, which addresses a key challenge faced by other sorbents. All these attributes make Li_3BO_3-based sorbents suitable for CO_2 capture from flue gas in post-combustion scenarios, such as fossil fuel-fired power plants, natural gas combined cycle power plants and other industrial flue gas streams. Recently, a more detailed analysis of the main intrinsic and operational properties of Li_3BO_3 compared with other sorbents for CO_2 capture has been reported [27–29]. Moreover, tri-lithium borate has demonstrated promising properties as a material for battery technology [30–33]. In fact, Li_3BO_3 has been selected as a key additive in the composite electrode production due to its low-melting and high lithium-ion conductivity, which increase the concentration of Li^+ in the contact layer with the solid electrolyte.

The carbonation of Li_3BO_3 proceeds via a solid-gas reaction that results in the formation of lithium carbonate (Li_2CO_3) and $Li_6B_4O_9$ as a lithium borate byproduct. The overall reaction is expressed as [27]:

$$4\,Li_3BO_{3\,(s)} + 3\,CO_{2\,(g)} \rightarrow 3\,Li_2CO_{3\,(s)} + Li_6B_4O_{9\,(s)}$$

The enthalpy change of the Li_3BO_3 carbonation to $Li_6B_4O_9$ ($\Delta H = 58 \pm 5$ kJ/mol) and the relationship between equilibrium CO_2 partial pressure and temperature for Li_3BO_3 has recently been determined [28]. This relationship primarily governs the working capacity of the material and the energy required for regeneration, both of which are critical for large-scale operations. The carbonation of Li_3BO_3 initiates with CO_2 chemisorption on lithium cation sites, followed by nucleation and growth of Li_2CO_3 at the surface of the particles. The process can become diffusion-limited due to the formation of a passivating product layer, which impedes further access of CO_2 to the reactive core. A potential solution involves the use of alkali metal additives such as nitrates, as they have shown to enhance carbonation kinetics by promoting the formation of molten phases [28,29]. Also, recent studies indicate that Li_3BO_3 carbonation may follow distinct pathways based on the CO_2 concentration [29], with different borate phases stabilizing depending on partial pressure conditions. Such behaviour underscores the need for comprehensive mechanistic studies capable of resolving phase-selective reaction dynamics.

While thermogravimetric analysis (TGA) and ex situ X-ray diffraction (XRD) studies have provided valuable insights into the carbonation performance of this material, they offer only limited temporal and structural resolution. In contrast, in situ time-resolved synchrotron XRD enables real-time monitoring of phase transformations during both synthesis and carbonation, offering a powerful method to unveil the kinetic and thermodynamic parameters governing these processes [34–39]. In fact, time-resolved in situ synchrotron X-ray diffraction (SR-XRD) is a highly powerful technique for studying complex, multi-step solid-gas reactions such as the carbonation of Li_3BO_3, primarily because its exceptional sensitivity and temporal resolution can resolve phenomena that remain invisible to conventional laboratory-based XRD (Lab-XRD) [34–37,40–42]. The reaction kinetics often involve the rapid formation of intermediate or transient phases and a passivating product layer, where crucial phases might only exist for seconds, or appear in very low concentrations (below the typical 2% detection limit of Lab-XRD). The high brilliance and intensity of synchrotron radiation allow for extremely fast data acquisition times, enabling the monitoring of these dynamic changes in real-time, thus capturing fleeting intermediate species and subtle structural shifts (e.g., lattice parameter variations). Moreover, the high signal-to-noise ratio and superior resolution of SR-XRD patterns mean that minor crystalline components, which produce peaks too weak or broad to be reliably detected with Lab-XRD, are clearly identifiable. This capability is particularly vital for mechanistic studies exploring different reaction pathways under varying partial pressures, providing a comprehensive understanding of the reaction dynamics that traditional XRD simply cannot achieve.

The primary goal of this investigation is to establish a rigorous baseline understanding the carbonation of pristine Li_3BO_3 using in situ time-resolved synchrotron X-Ray diffraction measurements combined with Rietveld analysis, which is currently lacking in the literature. The complex phase transformations occurring during both synthesis and carbonation of pure Li_3BO_3 needed to be systematically elucidated before additional variables could be meaningfully studied. In particular, we investigate the CO_2 capture behaviour of Li_3BO_3 under two distinct gas flow conditions: (i) 10% CO_2 balanced with an inert gas, selected to closely replicate post-combustion flue gas environments relevant to real-world carbon capture applications, and (ii) pure CO_2 (100%), used to evaluate the material's intrinsic reactivity and maximum uptake capacity. These distinctive atmospheres enable a detailed assessment of how CO_2 partial pressure influences key performance metrics, including the carbonation onset temperature, reaction kinetics, product phase composition, and process reversibility. By elucidating the coupled effects of temperature and CO_2 partial pressure on phase evolution and reaction dynamics, this work provides fundamental insights of Li_3BO_3 carbonation mechanism, which is essential for the rational design and operation of this promising sorbent material for high-efficiency carbon capture applications.

2. Experimental

2.1. Synthesis of tri-lithium borate

The starting materials are lithium carbonate (Li_2CO_3, Cicarelli pro analysis) and boric acid (H_3BO_3, Anedra ACS). The synthesis of Li_3BO_3 involves two steps, according to a procedure reported elsewhere [28]. First, a mixture of 3:2 molar ratio of Li_2CO_3:H_3BO_3 was weighted and placed in a stainless-steel mill chamber. This starting mixture was ball milled in air for 30 min at 400 RPM using a planetary mill (Fritsch Pulverisette 6) and a ball to powder mass ratio of 40:1. In the second step, the as-milled sample was heated at 5 °C/min from r.t. to 600 °C and kept at this temperature during 1 h.

2.2. Thermal and microstructural characterization

Thermal behaviour of the as-milled $3Li_2CO_3$-$2H_3BO_3$ mixture during heating in air (50 mL/min of synthetic air, 5 °C/min) was followed by simultaneous Differential Scanning Calorimetry and Thermogravimetry techniques (DSC-TG, Linseis PT-1600) coupled to a mass spectrometer (MS, ThermoStar Pfeiffer). Morphology and particle size of Li_3BO_3 were examined after synthesis and at the end of the carbonation reaction using Scanning Electron Microscopy (SEM, SEM-FIB, Zeiss, Crossbeam 340). The non-conductive powders were dispersed on a carbon tape and coated by gold sputtering to avoid charging effects. The elemental composition was determined by Energy Dispersive X-ray Spectroscopy (EDXS). Elemental mappings of the powders were obtained to characterize the carbon distribution.

2.3. CO_2 sorption properties

Thermogravimetry (TG) combined with differential scanning calorimetry (DSC) were used to analyse the non-isothermal reaction of Li_3BO_3 in CO_2 flow using 10 vol% or 100% CO_2 (Linseis STA PT-1600). The low CO_2 concentration was selected to simulate real-world conditions in post combustion applications. Isothermal carbonation and regeneration curves of Li_3BO_3 were obtained using TG (TG-HP50, TA Instruments) in CO_2/inert flow at 600 °C. First, a non-isothermal carbonation was performed from r.t to 600 °C under pure CO_2. Second, at constant temperature, the gas was switched to an inert gas and the regeneration step was measured (not shown). After that, successive carbonation/regeneration cycles at a fix temperature were performed in CO_2/inert atmosphere up to complete 10 cycles.

2.4. In situ synchrotron X-ray diffraction

In situ synchrotron XRD experiments were conducted at the BM01 of the Swiss-Norwegian beamline (SNBL) of the European Synchrotron Radiation Facility (ESRF). Both Li_3BO_3 synthesis and its carbon capture performance were studied using the experimental setup previously described by the authors [43]. Powder samples were thoroughly mixed and loaded into quartz capillaries with an inner/outer diameter of 0.9/1.0 mm. The capillaries were then mounted horizontally on a goniometer head connected to a spinning stage, enabling continuous sample rotation between 0 and 180°, and inserted in a horizontal furnace available at the beamline [44].

Different heat treatments were applied to the samples. For the synthesis study, a powder mixture consisting of $LiB_5O_8{\cdot}5H_2O$-Li_2CO_3, which was produced by the milling of H_3BO_3 and Li_2CO_3 powder reagents as described in Section 2.1, was subjected to a heating ramp of 5 °C/min from r.t until 600 °C. The dynamic CO_2 capture and thermal behaviour of Li_3BO_3 were examined under two different CO_2 flows (10 vol% or 100% CO_2, 10 cm^3/min), heating the sample up to 800 °C at a heating ramp of 5 °C/min.

The raw diffraction data obtained during the in situ experiments are available via the ESRF data portal [45]. The measurements were performed using a monochromatic X-ray beam (0.720 Å wavelength) with a beam size of 300 μm × 300 μm. Diffraction data were collected using a Dectris Pilatus 2 M photon-counting area detector, acquiring one frame every 30 s with an exposure time of 5 s per frame. Pictures of the experimental setup are shown in Fig. S1 of the Supplementary Material. Calibration was conducted using LaB_6 powder standard. The 2D XRD data were integrated using the Dioptas software [46], and posterior sequential Rietveld refinements were carried out using the FullprofApp, a FullProf-based software [47,48].

3. Results and discussion

3.1. Synthesis of Li_3BO_3 from Li_2CO_3 + H_3BO_3 mixture

3.1.1. Thermal analysis studies and morphological changes during Li_3BO_3 formation

In our previous investigation, we reported the synthesis of Li_3BO_3 from Li_2CO_3 and H_3BO_3 powder mixture by a two-step procedure in air [28]. This method consists of a first step of mechanical milling (MM) of $3Li_2CO_3$:$2H_3BO_3$ mixture for 30 min, followed by a second step of thermal treatment (TT) for 1 h at 600 °C. The overall reaction is represented by:

$$3\,Li_2CO_{3\,(s)} + 2\,H_3BO_{3\,(s)} \rightarrow 2\,Li_3BO_{3\,(s)} + 3\,CO_{2\,(g)} + 3\,H_2O_{(g)} \quad (1)$$

In the first step, the XRD pattern obtained reveals the presence of peaks corresponding to unreacted Li_2CO_3, as well as the most intense reflections of $LiB_5O_8{\cdot}5H_2O$ (Fig. S2a), indicating its formation during milling. Considering that the starting mixture of Li_2CO_3 and H_3BO_3 has a molar ratio of 3:2, an amount of Li_2CO_3 remains unreacted. The mechanochemical processing favors both the mixing and chemical interaction of the precursors. In fact, the formation of $LiB_5O_8{\cdot}5H_2O$ is clearly established after milling of $3Li_2CO_3$:$2H_3BO_3$ according to reaction (2), while the synthesis Li_3BO_3 occurs during the heating step via reaction (3) [28]:

$$0.2\;Li_2CO_{3\,(s)} + 2\;H_3BO_{3\,(s)} \rightarrow 0.4\;LiB_5O_8{\cdot}5\;H_2O_{(s)} + 0.2\;CO_{2\,(g)} + H_2O_{(g)} \quad (2)$$

$$0.4\;LiB_5O_8{\cdot}5\,H_2O_{(s)} + 5\;H_2O_{(g)} + 2.8\;Li_2CO_{3\,(s)} \rightarrow 2\;Li_3BO_{3\,(s)} + 2.8\;CO_{2\,(g)} + 7\;H_2O_{(g)} \quad (3)$$

Our synthesis of Li_3BO_3 by a two-step method involves a short milling time (30 min at room temperature) and a short thermal treatment at moderate 600 °C (1 h). These conditions are milder than those reported in previous studies [49,50]. In addition, the combination of milling and heat treatment results in an efficient method for producing Li_3BO_3 based sorbents: is sustainable (avoiding the use of chemical solvents), energy-efficient, scalable and flexible, due to its easily transfer from the laboratory to bulk production and adaptability to different raw materials [51–53].

Thermal analysis of the pre-milled mixture (Fig. 1) shows that the formation of Li_3BO_3 during heating up to 600 °C is a multi-step process. This can be inferred from the three stages of weight loss as well as multiple endothermic peaks upon heating observed in the TG-DSC curves. The first weight loss stage (step 1) correlates with the endothermic peak ending at 200 °C, which are associated with partial dehydration of $LiB_5O_8{\cdot}5H_2O$ [54]. This observation is in agreement with the MS signal corresponding to water detected in this temperature range. Next, between 200 °C and 420 °C (step 2), a slow weight loss is ascribed to the evolution of strongly bonded water between 200 °C and 300 °C, and the simultaneous CO_2 evolution from 250 °C (see MS signals). Finally, in the 420–600 °C temperature range, a sudden weight loss is observed (step 3) due to the complete reaction of Li_2CO_3 and residual Li-B-O compounds. In this temperature range, the formation of different borates of the Li_2O-B_2O_3 system is possible, with progressive CO_2 evolution [55]. The observation of multi endothermic peaks, which

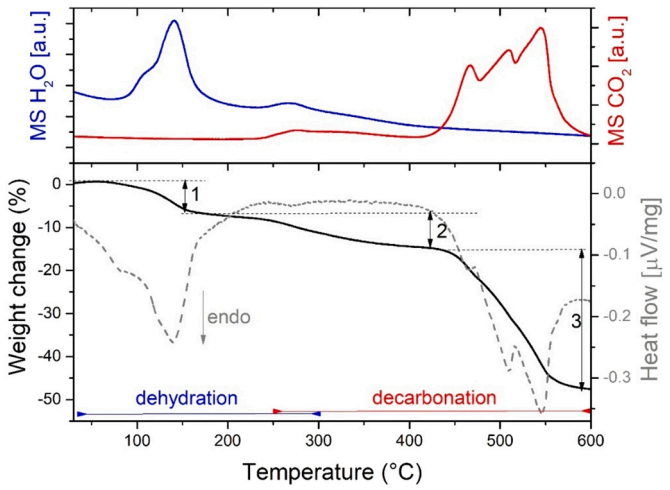


Fig. 1. TG-DSC-MS curves of $3Li_2CO_3$-$2H_3BO_3$ pre-milled mixture during heating in air flow (ramp 5 °C/min) from r.t. to 600 °C. MS signals correspond to $m/z = 18$ (H_2O) and $m/z = 44$ (CO_2).

correlate with CO_2 MS signal, reinforces the idea of the occurrence of multiple reactions. Thermal treatment of the pre-milled mixture for 1 h at 600 °C is sufficient to synthesize Li_3BO_3 as a single-phase product, as shown in Fig. S2b.

3.1.2. *In situ synchrotron diffraction studies during Li_3BO_3 formation*

To determine the Li_3BO_3 synthesis pathway from the pre-milled $3Li_2CO_3$-$2H_3BO_3$ mixture, the reaction was studied in situ via synchrotron X-ray diffraction. The aim of this study is to identify in real time the phases that are formed and the reaction intermediates, contributing to a better understanding of the system and the relative stability of the phases in this complex reaction system. Contour plots of Fig. 2a show the evolution of a selected 2θ region of the XRD patterns during the synthesis reaction. At the beginning of the thermal treatment, the previously mentioned Li_2CO_3 and $LiB_5O_8{\cdot}5H_2O$ are clearly observed in the XRD patterns. As the temperature increases, the reflections corresponding to $LiB_5O_8{\cdot}5H_2O$ gradually weaken and vanish around 170 °C, in agreement with the known dehydration behaviour of hydrated borates. Meanwhile, Li_2CO_3 reflections remain unchanged. This behaviour correlates with the first weight loss step due to dehydration process (Fig. 1).

In the mid-range temperature region, up to 450 °C, no significant changes are evidenced. This stage coincides with the second weight loss step (Fig. 1), where both water and CO_2 releasing were detected. According to Rousse et al. [56], other lithium borate phases such as $Li_3B_{11}O_{18}$, $Li_2B_4O_7$, or $Li_4B_2O_5$ could potentially crystallize in this compositional and thermal window, particularly from the boron-rich region of the Li_2O–B_2O_3 phase diagram. However, in the present study, no additional crystalline phases are detected during this interval, indicating that the reaction proceeds through either amorphous or nanocrystalline intermediates that remain undetectable by XRD. Between approximately 450 °C and 500 °C, new reflections appear in the diffraction patterns that do not match any known lithium borate or carbonate phases. The precise identification of this intermediate phase observed between 450 and 500 °C remains a challenge, as it emerges transiently and overlaps with coexisting phases, which makes is unambiguous identification extremely challenging. Under these conditions, the available data do not provide sufficient resolution or phase purity to reliably assign a space group or fully solve the crystal structure. The presence of this phase highlights the intricate reaction kinetics of the Li_3BO_3 system, a finding not previously observed in conventional ex situ studies, and represents an exciting avenue for future, highly specialized investigations. In addition, the emergence of this intermediate suggests a complex multi-step reaction mechanism, involving not only amorphous transformations but also a distinct crystalline precursor to the final product.

The formation of Li_3BO_3 is first evidenced by the appearance of its characteristic reflections at approximately 500 °C, as seen in the upper section of the contour plot in Fig. 2a. These reflections increase steadily in intensity with temperature, indicating a progressive crystallization process. The corresponding thermal profile shown in Fig. 2b confirms that the formation of Li_3BO_3 occurs during the high-temperature segment of the experiment, consistent with the thermally activated nature of the final step in the solid-state reaction. The complex structural evolution observed in the temperature range between 450 °C and 600 °C is in agreement with the results obtained from the TG-DSC-MS study (Fig. 1), where the occurrence of multiple reactions is also inferred.

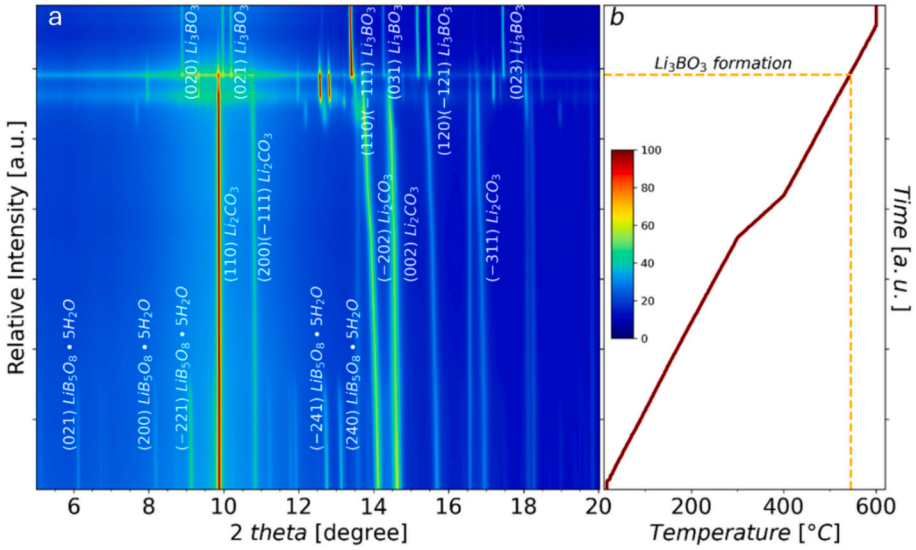


Fig. 2. (a) Contour plot showing the evolution of in situ synchrotron XRD patterns during the solid-state synthesis of Li_3BO_3 from a ball-milled Li_2CO_3 and H_3BO_3 mixture, with labelled reflections corresponding to $LiB_5O_8{\cdot}5H_2O$, Li_2CO_3, and Li_3BO_3. (b) Corresponding temperature profile applied during the experiment, indicating the onset of Li_3BO_3 crystallization.

3.2. Carbonation studies of Li_3BO_3 under CO_2 gas flow

3.2.1. Thermal analysis studies during Li_3BO_3 carbonation

Dynamic carbonation/decarbonation of the as-synthesized Li_3BO_3 was carried out using TG-DSC to compare the performance under different CO_2 pressures. Two different experimental conditions were selected based on their practical relevance: 10% CO_2, representative of post-combustion flue gas, and 100% CO_2, which provides the maximum driving force and then the upper benchmark for uptake capacity. The weight change curves were obtained by heating from r.t. to 650 °C under pure CO_2 and 10% of CO_2 (Fig. 3a). An initial slight weight gains from r.t. to 450 °C is observed for Li_3BO_3 sorbent due to superficial CO_2 sorption. This stage is followed by a sharp weight gain due to Li_3BO_3 carbonation, with the maximum CO_2 uptake shifting to higher temperatures with increasing CO_2 pressure (546 °C and 587 °C for 10% of CO_2 and pure CO_2, respectively). As expected, both the carbonation rate and the total CO_2 uptake are significantly enhanced under pure CO_2, reaching ~40 wt% compared to ~9 wt% under 10% CO_2.

Following the carbonation peak, a decarbonation step is observed in both conditions. The faster CO_2 desorption rate under 10% CO_2 is consistent with the predicted shift in the equilibrium decomposition temperature based on CO_2 partial pressure. According to the equilibrium analysis of gas–solid reactions, such as those developed for Li_4SiO_4-based systems [57], the decomposition of carbonate phases is favoured at lower CO_2 partial pressures, where the chemical potential of CO_2 is reduced. These are the most common experimental conditions for sorbent regeneration in post-combustion scenarios, which generally involve high temperatures and a controlled CO_2 stream, being possible to select different CO_2 concentrations and temperatures depending on the thermodynamic of the sorbent [57–60]. Alternatively, instead of CO_2 flow an inert purge gas like N_2 could be used.

The thermal phenomena observed in the DSC curves (Fig. 3b) have a good correlation with the carbonation/decarbonation processes identified by TG, although some differences are identified. As carbonation progress, an increasing heat flow slope with apparent peaks at 485 °C and 520 °C (525 °C and 567 °C) for 10% of CO_2 (pure CO_2) were observed due to the carbonation process. Beyond ~520 °C (557 °C), a stronger endothermic peak at ~569 °C (630 °C) is evident for 10% of CO_2 (pure CO_2), which is associated with the CO_2 release. Although TG curves indicate that the carbonation is a progressive and continuous reaction, thermal behaviour shows more than one exothermic peak. This observation can be related with the occurrence of an endothermic event whose characteristic peak overlaps with the exothermic peak of the carbonation. Experimental evidence suggests that the endothermic peak is due to the formation of a molten phase at the surface. In a previous study on the carbonation of un-doped Li_4SiO_4, a similar thermal behaviour was observed and attributed to the presence of a molten phase [61].

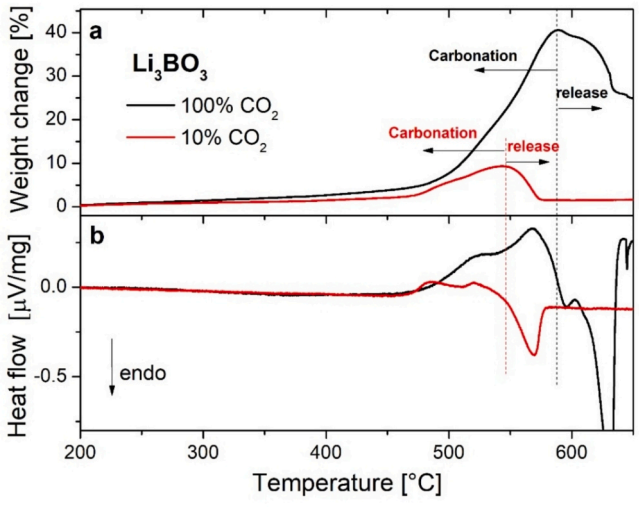


Fig. 3. a) TG and b) DSC curves of as-synthesized Li_3BO_3 during heating under pure CO_2 and 10% of CO_2 flow (ramp 5 °C/min) from r.t. to 700 °C.

The cyclic reversibility of Li_3BO_3 is possible under different experimental conditions based on the relationship between CO_2 equilibrium pressure and temperature [28]. Successive cycles of carbonation of Li_3BO_3 and regeneration at 600 °C were measured under pure CO_2/inert gas flow (Fig. S3). It can be inferred that as the cycling progresses, a reduction in the CO_2 capture capacity is observed, decreasing from 38 wt % to 35 wt% after 10 cycles.

The morphology of the as-synthesized Li_3BO_3 (Fig. 4a–c) and as-carbonated Li_3BO_3 under 10% of CO_2 and pure CO_2 (Fig. 4d–i) was examined using SEM. Although both Li_2CO_3 and H_3BO_3 powders precursors have very different initial sizes and shapes (platelets versus grains, see Fig. S4), the mechanochemical processing produces an intimate and homogeneous mixture of them forming $LiB_5O_8{\cdot}5H_2O$ (Fig. S5). In fact, mechanical milling favors the interaction between the reagents both during milling and further solid-state reaction upon heating. Formation of Li_3BO_3 as final phase generates a new microstructure which looks like a porous network slightly intertwined (Fig. 5b), probably promoted by the evolution of gaseous species during heating and the use of low temperature/short time of thermal treatment. This interconnected structure is composed of small and rounded grains of ~1 μm (Fig. 4c), with a smooth surface and a macropore size that would facilitate CO_2 sorption. After carbonation at 530 °C and 570 °C (Fig. 4d and g, respectively), the interconnected structure looks sintered and seems to be held together by a liquid phase. Detailed examination of the surface reveals faceted crystals with straight edges and sizes ranging from 100 nm to 1 μm, which are related with Li_2CO_3 phase (Fig. 4e, f, h and i). The higher degree of carbonation reached at 570 °C with pure CO_2 promotes the growth of Li_2CO_3 crystals forming a framework of macropores. The elemental mapping of C, B and O shows homogeneous distribution of Li-B-O and Li_2CO_3 compounds at the surface, as it can be inferred by comparison of carbon and boron distribution (Fig. S6). Successive sorption cycles at 600 °C induce grain sintering and crystal growth of Li_2CO_3 (Fig. S7). These microstructural changes could be considered the main reason of the deterioration in the CO_2 capture capacity with cycling. These observations are in agreement with the microstructural features reported after sorption cycles of undoped-Li based sorbents [27,28,34].

3.2.2. In situ synchrotron diffraction studies during Li_3BO_3 carbonation under 10% CO_2 gas flow

The evolution of the diffraction patterns during the carbonation of Li_3BO_3 under a 10% CO_2 atmosphere and the corresponding temperature profile are displayed in Fig. 5a and b, respectively. At the beginning of the experiment, the pattern is dominated by reflections from the initial Li_3BO_3 phase. Upon heating, the first indications of carbonation are observed at approximately 350 °C, where weak reflections corresponding to Li_2CO_3 begin to appear. The amount of Li_2CO_3 remains low up to about 450 °C, suggesting that the carbonation reaction proceeds slowly at this stage under limited CO_2 partial pressure. This first stage correlates with the superficial carbonation identified in TG measurements (Fig. 3a).

Above 450 °C, the intensity of Li_2CO_3 reflections increases. In this same temperature range, new peaks attributed to $Li_6B_4O_9$ become visible around 520 °C, indicating the formation of lithium borate by-products as secondary reaction products. The phase fraction of $Li_6B_4O_9$ increase progressively with the carbonation, with a maximum at 580 °C before the beginning of decarbonation. Additionally, a third crystalline phase emerges, corresponding to a lithium boron carbonate solid solution of general formula $Li_{(2+x)}C_{(1-x)}B_xO_3$. This phase grows in parallel with Li_2CO_3 and becomes increasingly prominent above 530 °C, likely indicating partial boron incorporation into the carbonate matrix

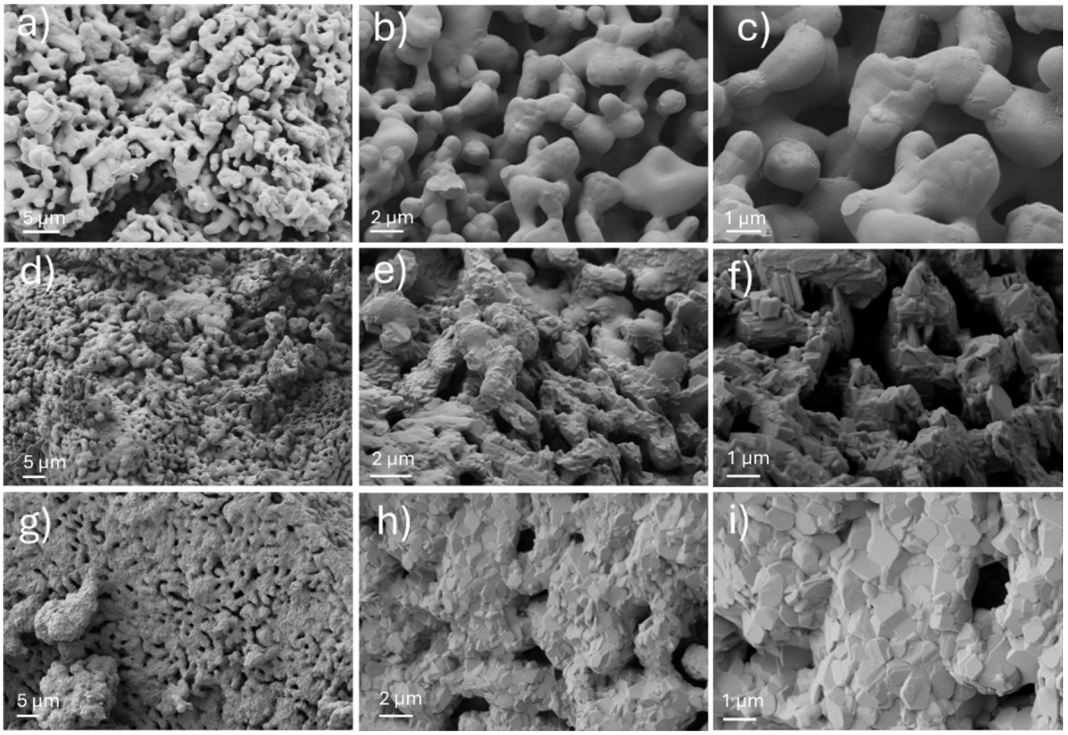


Fig. 4. SEM micrographs of: (a–c) as-synthesized Li_3BO_3; (d–f) Li_3BO_3 after carbonation under 10% CO_2 at 530 °C; (g–i) Li_3BO_3 after carbonation under 100% CO_2 at 570 °C.

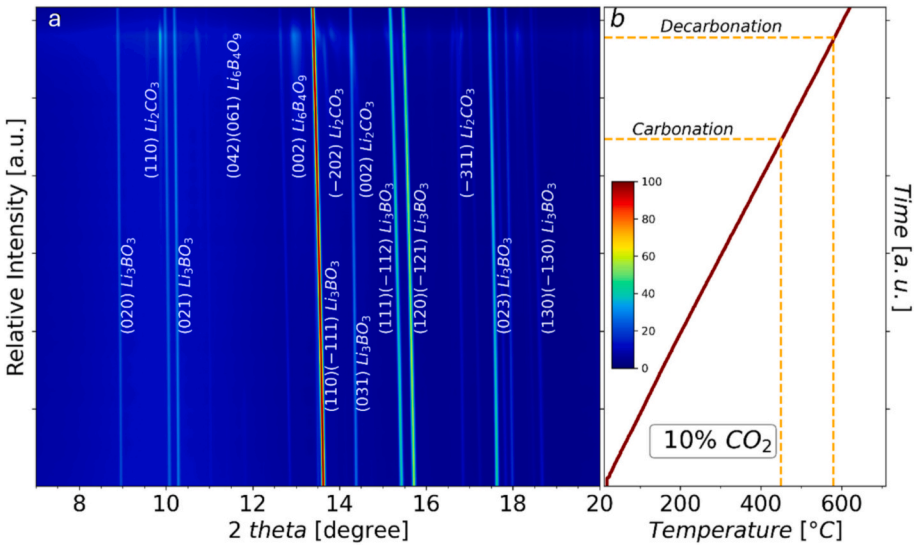


Fig. 5. a) Contour plots of in situ synchrotron XRD patterns collected during the carbonation of Li_3BO_3 under 10% of CO_2, b) corresponding temperature profiles.

or the formation of a structurally disordered boron-containing carbonate phase. To the authors' knowledge, this is the first time that the solid solution $Li_{(2+x)}C_{(1-x)}B_xO_3$ was detected during carbonation of Li_3BO_3. Although other phases are simultaneously present with the $Li_{(2+x)}C_{(1-x)}B_xO_3$ solid solution, its crystal structure is distinct enough to be clearly identified and the signal quality is sufficient to achieve a high quality of fit of the XRD pattern.

Fig. 6 displays the evolution of crystalline phases during the carbonation of Li_3BO_3 under 10% of CO_2, as determined by in situ synchrotron XRD and Rietveld analysis. The diffraction pattern collected at 200 °C (Fig. 6a) confirms the presence of unreacted Li_3BO_3 with negligible signs of product formation. At 540 °C (Fig. 6b), the emergence of reflections corresponding to Li_2CO_3 and $Li_6B_4O_9$ marks the progression of carbonation, with these phases coexisting with the parent borate. Further heating to 580 °C (Fig. 6c) results in a complex pattern featuring Li_2CO_3 and $Li_6B_4O_9$, while signatures of the mixed carbonate-borate solid solution $Li_{(2+x)}C_{(1-x)}B_xO_3$ are clearly detected. At 620 °C (Fig. 6d), the diffraction pattern shows a pronounced decrease in Li_3BO_3 intensity and dominance of Li_2CO_3, indicating near-complete decarbonation.

The corresponding phase fraction plot (Fig. 6e) reveals that Li_2CO_3 formation initiates at approximately 350 °C, and its fraction remains below 5% up to 450 °C. A more pronounced growth is observed at higher temperatures, reaching around 15% at 550 °C. $Li_6B_4O_9$ appears at

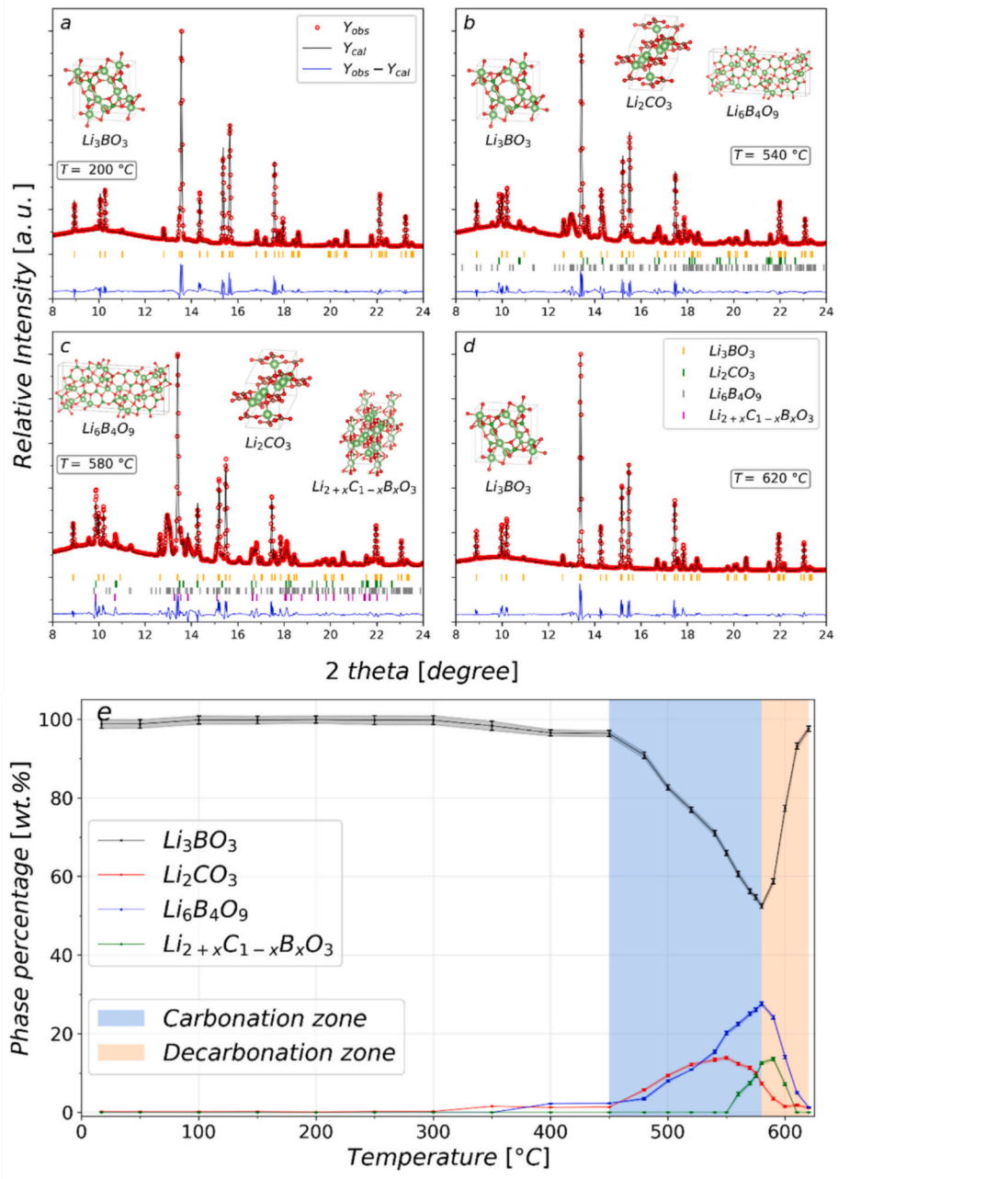


Fig. 6. Selected in situ XRD patterns during Li_3BO_3 carbonation under 10% CO_2 at (a) 200 °C, (b) 540 °C, (c) 580 °C, and (d) 620 °C, with corresponding Rietveld refinements. (e) Phase fraction evolution as a function of temperature, derived from sequential Rietveld analysis.

400 °C and increases steadily, peaking near 580 °C, indicating its role as a major intermediate product during carbonation. Its persistence over a broad temperature range suggests a stable transformation pathway under 10% CO_2. In contrast, the $Li_{(2+x)}C_{(1-x)}B_xO_3$ solid solution emerges at around 550 °C and reaches its maximum fraction near 580 °C. The temperature-dependent evolution of $Li_6B_4O_9$ and $Li_{(2+x)}C_{(1-x)}B_xO_3$ indicates that carbonation under 10% CO_2 does not follow a single reaction pathway but rather proceeds through a complex sequence involving competitive and possibly sequential formation of multiple crystalline products. These observations support the occurrence of the following reactions during dynamic carbonation:

$$4\ Li_3BO_{3\ (s)} + 3\ CO_{2\ (g)} \rightarrow 3\ Li_2CO_{3\ (s)} + Li_6B_4O_{9\ (s)}\ (400\text{–}580\ ^\circ C) \quad (4)$$

$$x\ Li_3BO_{3\ (s)} + (1-x)\ Li_2CO_{3\ (s)} \rightarrow Li_{(2+x)}C_{(1-x)}B_xO_{3\ (s)}\ (530\text{–}580\ ^\circ C) \quad (5)$$

These results highlight the significant impact of CO_2 partial pressure on the reaction mechanism. Under 10% CO_2, the carbonation of Li_3BO_3 is incomplete, and the product distribution indicates the coexistence of multiple reaction networks, likely governed by kinetic limitations and phase metastability within the temperature range studied. As temperature increases above 580 °C under 10% of CO_2, desorption of CO_2 is favoured from Li_2CO_3 and $Li_{(2+x)}C_{(1-x)}B_xO_3$ with the simultaneous formation of Li_3BO_3 via the reverse reactions (4) and (5). The progressive formation and consumption of the $Li_{(2+x)}C_{(1-x)}B_xO_3$ in the temperature range from 530 °C to 610 °C, demonstrates that the solid solution can be regenerated.

3.2.3. *In situ synchrotron diffraction studies during Li_3BO_3 carbonation under pure CO_2 flow*

To analyse the effect of the partial pressure on the structural changes that occurs during carbonation, in situ synchrotron XRD studies were

also performed under pure CO_2. The contour plot of Fig. 7a shows the evolution of XRD patterns during the carbonation of Li_3BO_3 under a pure CO_2 flow, together with the corresponding temperature evolution (Fig. 7b). In contrast to the behaviour observed under 10% CO_2, the reaction proceeds more rapidly and begins at a significantly lower temperature. Reflections corresponding to Li_2CO_3 appear already at approximately 300 °C, indicating an earlier onset of carbonation. Between 300 °C and 400 °C, the Li_2CO_3 phase fraction increases gradually, suggesting that even at low temperatures, the high CO_2 partial pressure effectively drives the initial stages of the reaction.

Fig. 8a–d presents selected in situ synchrotron XRD patterns and Rietveld refinements collected during the dynamic carbonation of Li_3BO_3 at temperatures representative of key stages of the reaction. At 200 °C, Li_3BO_3 the predominant phase, with minor reflections attributable to Li_2CO_3, indicating incipient surface carbonation. Upon heating to 450 °C, the formation of $Li_6B_4O_9$ becomes evident, surpassing Li_2CO_3 in phase fraction, thus confirming its role as a major carbonation product at intermediate temperatures. At 550 °C, a more complex multiphase mixture is observed, with Li_3BO_3, Li_2CO_3, $Li_6B_4O_9$, and $LiBO_2$ coexisting. Notably, $LiBO_2$ appears as a secondary product at elevated temperatures and persists throughout further heating. At 580 °C, the diffraction data reveal the emergence of a lithium boron carbonate solid solution, denoted as $Li_{2+x}C_{1-x}B_xO_3$, characterized by partial substitution of carbonate by borate and the incorporation of excess lithium.

Fig. 8e summarizes the evolution of all crystalline phases as a function of temperature. It can be clearly observed that Li_2CO_3 content increases sharply above 400 °C, reaching nearly 35% phase fraction at 550 °C. Simultaneously, weaker reflections emerge corresponding to secondary products such as $Li_6B_4O_9$ and $LiBO_2$, both of which exhibit more limited evolution compared to the dominant Li_2CO_3 phase. While $Li_6B_4O_9$ is detected from 300 °C, the formation of $LiBO_2$ is identified above 490 °C. The relative intensity of these by-products together with the increasing fraction of Li_2CO_3 compared to the 10% CO_2 case, suggests a higher degree of selectivity toward complete carbonation under pure CO_2 conditions. The parent phase, Li_3BO_3, begins to decline steadily after 300 °C and is nearly fully consumed by 600 °C. This complete conversion aligns with the stabilization of Li_2CO_3 as the predominant crystalline product, preceding the appearance of an amorphous halo above 600 °C in the contour plot (Fig. 7a). The emergence of $Li_{(2+x)}C_{(1-x)}B_xO_3$ is also detected above 550 °C, though it is less pronounced than in the low CO_2 experiment, indicating that boron incorporation into the carbonate matrix is less favoured under high CO_2 partial pressure. These results indicate that the carbonation of Li_3BO_3 proceeded by the following reactions:

$$4\ Li_3BO_{3\ (s)} + 3\ CO_{2\ (g)} \rightarrow 3\ Li_2CO_{3\ (s)} + Li_6B_4O_{9\ (s)}\ (350–600\ °C) \quad (6)$$

$$x\ Li_3BO_{3\ (s)} + (1-x)\ Li_2CO_{3\ (s)} \rightarrow Li_{(2+x)}C_{(1-x)}B_xO_{3\ (s)}\ (550–600\ °C) \quad (7)$$

$$Li_3BO_{3\ (s)} + CO_{2\ (g)} \rightarrow Li_2CO_{3\ (s)} + LiBO_{2\ (s)}\ (490–600\ °C) \quad (8)$$

$$Li_6B_4O_{9\ (s)} + CO_{2\ (g)} \rightarrow Li_2CO_{3\ (s)} + 4\ LiBO_{2\ (s)}\ (490–600\ °C) \quad (9)$$

The formation of $LiBO_2$ from 490 °C could occur through two alternative routes represented by the reactions (8) and (9). From a structural point of view, the sequence $Li_3BO_3 \rightarrow Li_6B_4O_9 \rightarrow LiBO_2$ is highly probable [56].

The phase evolution presented in Fig. 8e confirms that carbonation under pure CO_2 proceeds more efficiently, with a lower onset temperature, faster kinetics, and higher final conversion compared to the reaction under diluted conditions. The higher phase fraction of the secondary borates and mixed carbonate phases further indicates that high CO_2 partial pressure enhances both the thermodynamic driving force and the selectivity of the carbonation process, favouring the formation of Li_2CO_3 as the primary product. This study also shows that the decarbonation reaction is not observed up to 600 °C under dynamic heating conditions of pure CO_2 flow. Although the diffraction data do not reveal clear evidence of Li_2CO_3 decomposition below this temperature, TG-DSC measurements indicate that decarbonation onset occurs at approximately 590 °C under pure CO_2, a discrepancy that can be attributed to differences in system fluid dynamics and the distinct sensitivities of the in situ diffraction and thermal analysis techniques.

3.2.4. *Mechanism of Li_3BO_3 carbonation under different pressure of CO_2: role of $Li_{(2+x)}C_{(1-x)}B_xO_3$*

Fig. 9 illustrates the temperature ranges over which each crystalline phase is present during carbonation under different CO_2 pressures. Under 10% of CO_2 flow (Fig. 9a), the onset of carbonation is delayed, with the first appearance of Li_2CO_3 occurring around 350 °C. The parent Li_3BO_3 phase remains dominant up to approximately 450 °C, after which its intensity gradually decreases. As temperature increases, new phases emerge: $Li_6B_4O_9$ becomes detectable around 400 °C, and the formation of a boron-substituted carbonate phase, $Li_{(2+x)}C_{(1-x)}B_xO_3$, is also observed above 530 °C. The maximum consumption of Li_3BO_3 occurs

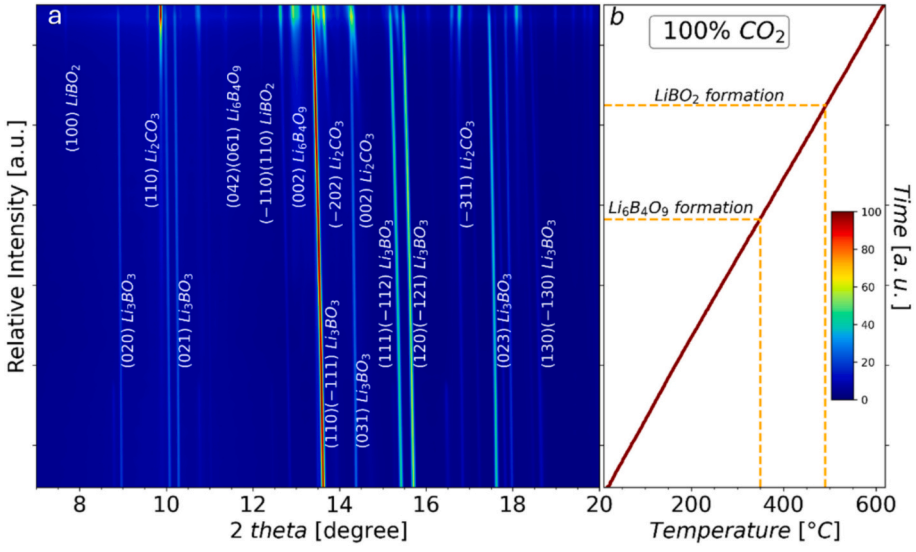


Fig. 7. (a) Contour plot displaying the evolution of in situ synchrotron XRD patterns during the dynamic carbonation of Li_3BO_3 under 100% CO_2 flow. (b) Corresponding linear temperature profile applied during the experiment.

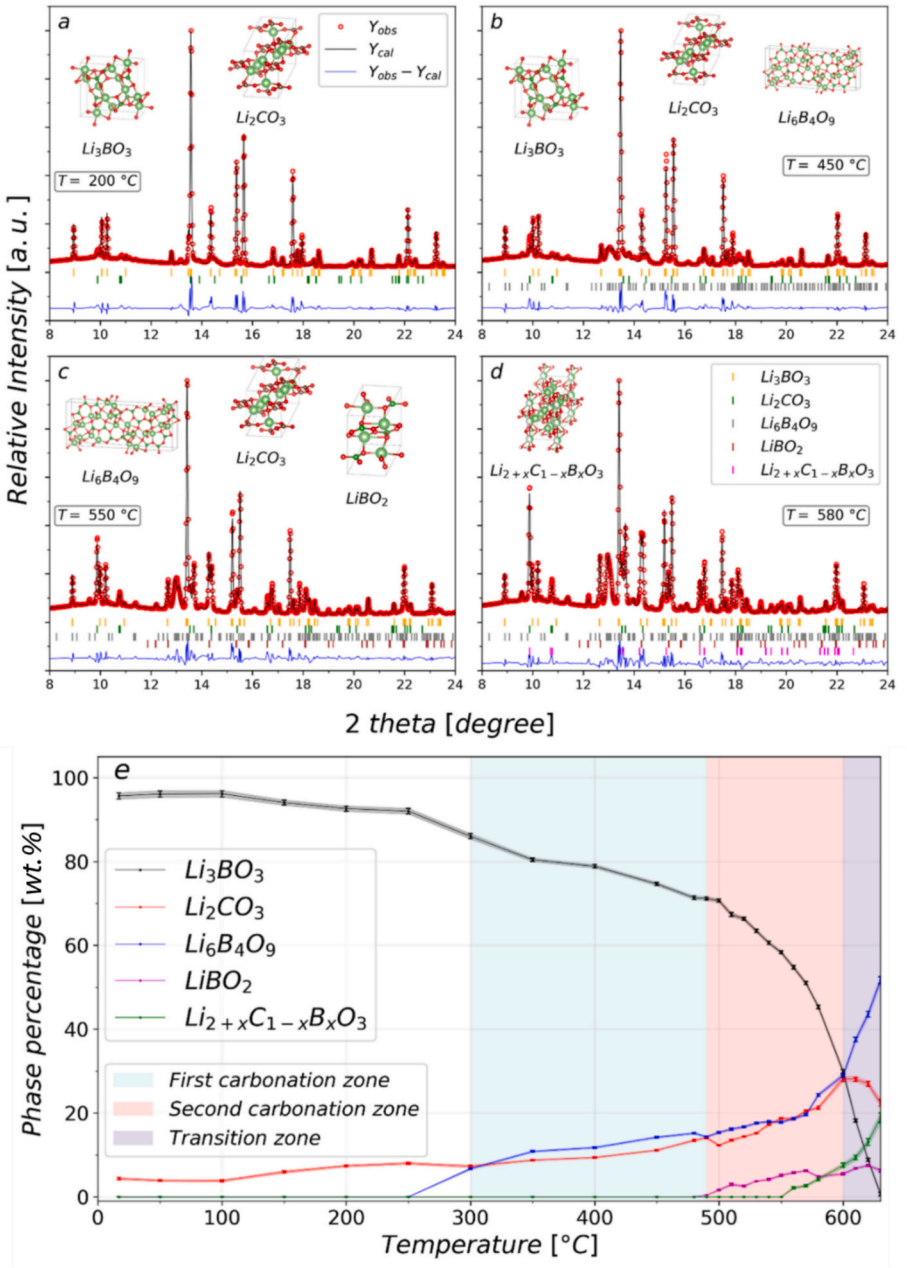


Fig. 8. Selected in situ XRD patterns during Li_3BO_3 carbonation under pure CO_2 at (a) 200 °C, (b) 450 °C, (c) 550 °C, and (d) 580 °C, with corresponding Rietveld refinements. (e) Phase fraction evolution as a function of temperature, derived from sequential Rietveld analysis.

near 580 °C, with the final phase assemblage including Li_2CO_3, $Li_6B_4O_9$, and $Li_{(2+x)}C_{(1-x)}B_xO_3$, indicating a multistep reaction pathway. Based on these results, the carbonation process would involve the following transformations (see reactions (4) and (5)):

$$Li_3BO_{3\,(s)} \rightarrow Li_2CO_{3\,(s)} + Li_6B_4O_{9\,(s)}$$

$$x\ Li_3BO_{3\,(s)} + (1-x)\ Li_2CO_{3\,(s)} \rightarrow Li_{(2+x)}C_{(1-x)}B_xO_{3\,(s)}$$

These reactions are initially in series, being Li_2CO_3 first formed between 400 and 520 °C and after some extension of carbonation, it reacts with Li_3BO_3 to produce the solid solution. From 530 °C to 580 °C, these reactions could occur simultaneously and be competitive, evidencing the complex pathway of carbonation. Above 580 °C, decarbonation proceeds and the evolution of the phases (Fig. 6) demonstrates that the previous carbonation reactions are reversible under 10% of CO_2.

In contrast, carbonation under pure CO_2 flow (Fig. 9b) initiates at a significantly lower temperature of 300 °C. The formation of Li_2CO_3 progresses rapidly, becoming the dominant crystalline phase before 500 °C. The Li_3BO_3 phase begins to diminish shortly after carbonation starts and it is almost entirely consumed by 600 °C. The formation of secondary borate phases like $Li_6B_4O_9$ and $LiBO_2$ is observed from 350 °C and 490 °C, respectively, being more pronounced than in the 10% CO_2 case. Therefore, dynamic carbonation under pure CO_2 shows the formation of two different lithium borates with temperature increasing (see reactions (6) and (9)):

$$Li_3BO_{3\,(s)} \rightarrow Li_6B_4O_{9\,(s)} \rightarrow LiBO_{2\,(s)}$$

Although $LiBO_2$ could be also formed by direct carbonation of Li_3BO_3, the progressive Li extraction from the tri-lithium borate structure is energetically more feasible, reinforcing this Li-B-O sequence [44,45]. Additionally, the signal corresponding to $Li_{(2+x)}C_{(1-x)}B_xO_3$ starts at higher temperatures (550 °C) and remains until 600 °C under

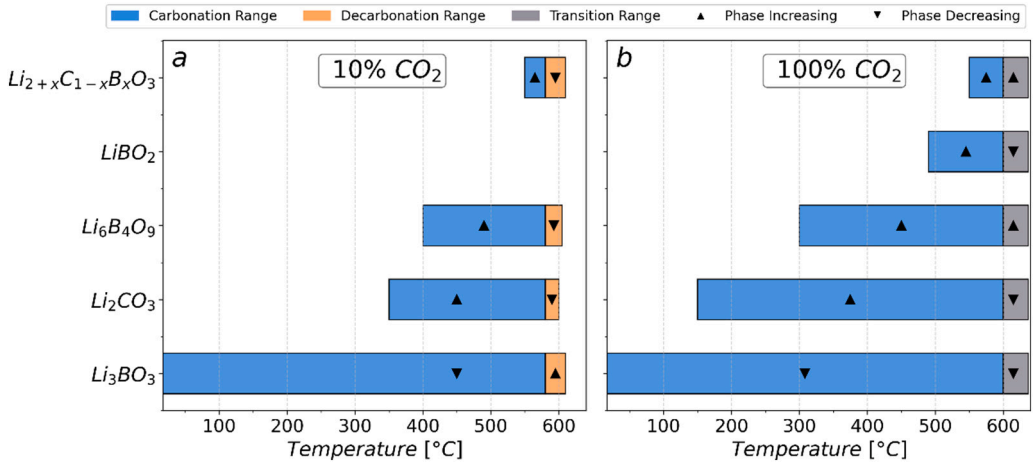


Fig. 9. Temperature ranges of observed crystalline phases during in situ carbonation reactions under: a) 10% CO_2 gas flow, b) 100% CO_2. The arrow indicates a progressive increase or decrease in the phase fraction with the increasing temperature.

pure CO_2. In this temperature range, the formation of $Li_{(2+x)}C_{(1-x)}B_xO_3$ requires Li_3BO_3 which also is consummated by reaction (6), i.e. kinetics factors determine the predominance of each reaction.

Based on the in situ XRD findings, a global carbonation mechanism is proposed. Initially, the carbonation of Li_3BO_3 starts with CO_2 adsorption on the surface, independently of the CO_2 pressure, leading to the formation of a thin layer of $Li_6B_4O_9$ and Li_2CO_3 on the external surface of the solid powders (Figs. 3, 6 and 8). The main difference between both CO_2 pressures lies in the driving force, and therefore in the extent of the surface reaction at a given temperature. At this stage, the chemical reaction is primarily controlled by kinetic factors. As temperature increases, the bulk carbonation proceeds and the solid fraction of $Li_6B_4O_9$ and Li_2CO_3 grows. The reaction progress at this stage requires the CO_2 diffusion and/or Li^+ and O^{2-} ion diffusion through the layer of the solid-state products, which may consist of two ($Li_6B_4O_9$ and Li_2CO_3) or three solid phases ($Li_6B_4O_9$, Li_2CO_3 and $LiBO_2$), depending on the CO_2 pressure. SEM observations show that Li_3BO_3 exhibits an interconnected microstructure with macropores, which seem to be linked by a liquid phase (Figs. 3 and 4). After about 30 wt% and 45 wt% of Li_3BO_3 consumption under 10% and 100% of CO_2 pressure, respectively, the formation of $Li_{(2+x)}C_{(1-x)}B_xO_3$ from solid-state reaction between Li_2CO_3 and unreacted Li_3BO_3 is promoted. This reaction kinetically competes with the progress of the Li_3BO_3 carbonation.

The in situ formation of $Li_{(2+x)}C_{(1-x)}B_xO_3$ during carbonation of Li_3BO_3 deserves a special analysis. These solid solutions were previously obtained by solid-state synthesis between Li_2CO_3 and small amount of Li_3BO_3 [62], being isostructural with Li_2CO_3 [63]. A previous study had reported that their Li-ion conductivity enhances from 10^{-7} to 10^{-3} S cm^{-1} at 200 °C as x in $Li_{(2+x)}C_{(1-x)}B_xO_3$ changes from 0 to 0.25. The maximum in the conductivity has been measured between x = 0.3 and 0.5 for 150 and 200 °C [63]. Fig. 10 shows the estimated evolution of x with the temperature for the $Li_{(2+x)}C_{(1-x)}B_xO_3$ solid solution during dynamic carbonation under 10% of CO_2. This analysis could not be performed for the 100% dataset, as the solid solution emerges at higher temperatures under these conditions and coexists with significant amounts of $LiBO_2$, which hinders reliable refinement of the occupancy parameters of $Li_{(2+x)}C_{(1-x)}B_xO_3$.

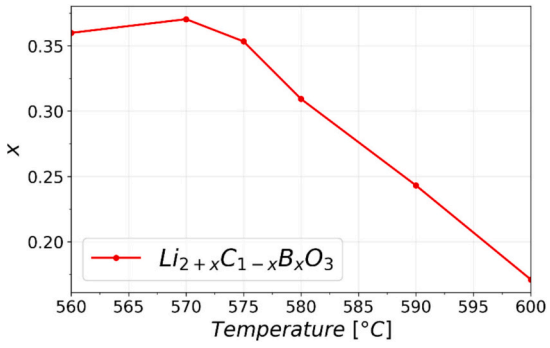


Fig. 10. Evolution of x in $Li_{(2+x)}C_{(1-x)}B_xO_3$ during dynamic carbonation under 10% of CO_2.

In all XRD patterns of the sample subjected to 10% CO_2, the $Li_{(2+x)}C_{(1-x)}B_xO_3$ phase was indexed considering that BO_3^{3-} ion substitutes CO_3^{2-} with the introduction of interstitial Li ion in the monoclinic phase of Li_2CO_3 (space group C12/c). The x value obtained shows a maximum at 570 °C (x = 0.38) and decreases with the temperature, while the maximum of the phase fraction is observed at 580 °C before the beginning of decarbonation. It is expected that the increase of x value induces an expansion along c axis by the formation of interstitial Li ion [63], with a beneficial effect on the conductivity values. This behaviour was confirmed by Okumura et al. [64], where the Li-ion conductivities measured for $Li_{(2+x)}C_{(1-x)}B_xO_3$ (x = 0.1–0.3) were hundred-thousand-fold of that for Li_2CO_3 and associated with the interstitial Li ion transfer in the monoclinic structure. Moreover, a detailed investigation about the structure of $Li_{(2+x)}C_{(1-x)}B_xO_3$ and Li ion migration pathways, supported by experimental and theoretical data, identifies different Li^+ migration mechanisms and reveals that the dominant one changes with temperature [65].

These features can be associated with previous studies where diffusion resistance of Li^+ and O^{2-} could be a limiting step for CO_2 sorption process [66–68]. In fact, at the beginning, surface CO_2 sorption on Li_3BO_3 generates Li-B-O compounds and Li_2CO_3 nuclei in the outside shell. Additional carbonation requires that CO_2 diffusion occurs across this shell to react with the fresh Li_3BO_3 sorption [28]. An alternative possibility is that Li^+ and O^{2-} ions should diffuse across the product layer to continue the carbonation. Therefore, improving the mobility of these ions is one effective option to enhance CO_2 sorption behaviour [11].

Overall, it can be observed that higher CO_2 partial pressure enhances the carbonation kinetics toward Li_2CO_3, forming $Li_6B_4O_9$ and $LiBO_2$, while lower CO_2 concentration leads to $Li_6B_4O_9$ evolution. Formation of boron-substituted carbonate species, with different x content, were favoured at different temperature ranges. This solid solution shows different stabilization range with the temperature and CO_2 partial pressure. Its formation could play a crucial role when carbonation kinetics is controlled by diffusion by improving the Li^+ ion mobility through Li_3BO_3-Li_2CO_3 interphase. These trends underscore the critical role of CO_2 partial pressure in governing both the thermodynamics and

reaction pathways during Li_3BO_3 carbonation.

4. Conclusions

Synthesis of Li_3BO_3 was performed by a two-step process: first, the mechanical milling of $3Li_2CO_3$-$2H_3BO_3$ mixture which produces $LiB_5O_8{\cdot}5H_2O$ as intermediate phase along with unreacted Li_2CO_3, followed by the thermal treatment of the as-milled mixture up to 600 °C. Time-resolved in situ synchrotron XRD analysis revealed that the as-milled mixture, consisting of $LiB_5O_8{\cdot}5H_2O$ and Li_2CO_3, is successfully transformed via a multi-step mechanism to Li_3BO_3, involving both amorphous and crystalline intermediates. In fact, between 450 °C and 550 °C, new reflections of an unidentified compound are observed in the XRD patterns. The main reflections from crystalline Li_3BO_3 are detected at about 500 °C. The global synthesis mechanism involves at least three steps of weight loss, with both H_2O and CO_2 releasing during heating from r.t. to 600 °C.

Structural changes during the dynamic carbonation of Li_3BO_3 from r. t. to 600 °C under 10% of CO_2 and pure CO_2 flow were investigated using in situ high-temperature synchrotron XRD combined with Rietveld analysis. Experimental results show that under 10% of CO_2 flow, Li_3BO_3 reacts with CO_2 to produce $Li_6B_4O_9$ and Li_2CO_3. At temperatures between 530 and 580 °C, uncarbonated Li_3BO_3 and Li_2CO_3 lead to the formation of $Li_{(2+x)}C_{(1-x)}B_xO_3$ solid solution. When pure CO_2 is used, the formation of $Li_6B_4O_9$ and $LiBO_2$ is identified, whereas the temperature range of $Li_{(2+x)}C_{(1-x)}B_xO_3$ stabilization is higher. The solid solution $Li_{(2+x)}C_{(1-x)}B_xO_3$ is recognized as an ionic conductor with high lithium ion mobility, so its presence can enhance carbonation kinetics.

The findings presented in this work underscore the critical role of the $Li_{2+x}C_{1-x}B_xO_3$ solid solution, particularly at elevated temperatures. The identification of distinct reaction pathways under 100% and 10% of CO_2, with the latter being closer to real application conditions, provides valuable insight into how operating atmosphere influences phase evolution and reactivity. This mechanistic understanding is essential for the rational design and optimization of Li_3BO_3-based materials as efficient, tuneable sorbents for high-temperature CO_2 capture under realistic conditions.

CRediT authorship contribution statement

María José Orozco: Writing – review & editing, Writing – original draft, Methodology, Investigation, Formal analysis, Data curation. **María Laura Grasso:** Writing – review & editing, Methodology, Investigation, Formal analysis, Data curation. **Pedro Alonso-Sánchez:** Writing – review & editing, Validation, Supervision, Methodology, Investigation, Formal analysis, Data curation. **Federico Cova:** Methodology, Investigation, Formal analysis, Data curation, Conceptualization. **María Laura Rodriguez:** Writing – review & editing, Resources, Conceptualization, Methodology, Data curation. **María Valeria Blanco:** Investigation, Funding acquisition, Formal analysis, Data curation, Conceptualization, Supervision, Writing – original draft, Writing – review & editing. **Fabiana C. Gennari:** Conceptualization, Funding acquisition, Investigation, Methodology, Supervision, Writing – original draft, Writing – review & editing.

Declaration of competing interest

The authors declare that they have no known competing financial interests or personal relationships that could have appeared to influence the work reported in this paper.

Acknowledgements

This work was supported by the Grant No PCI2022-132993 funded by MCIN/AEI/10.13039/501100011033, DGA/M4 from Diputación General de Aragón, and European Union “NextGeneration EU”/PRTR, by financial support of CNEA (the National Commission of Atomic Energy), ANPCyT - PICT 2021-1270 and the High Impact Federal Networks Project (CapCO2). Beamtime allocation at BM01 of ESRF trough the A01-2-1316 experiment and support from C. Fuller is also acknowledged.

Appendix A. Supplementary data

Supplementary data to this article can be found online at https://doi.org/10.1016/j.cej.2026.173902.

Data availability

we have shared an url to download the data

References

[1] R. Quadrelli, S. Peterson, The energy–climate challenge: recent trends in CO_2 emissions from fuel combustion, Energy Policy 35 (2007) 5938–5952, https://doi.org/10.1016/j.enpol.2007.07.001.
[2] X. Yu, C.O. Catanescu, R.E. Bird, S. Satagopan, Z.J. Baum, L.M. Lotti Diaz, Q. A. Zhou, Trends in research and development for CO_2 capture and sequestration, ACS Omega 8 (2023) 11643–11664, https://doi.org/10.1021/acsomega.2c05070.
[3] J.A. Garcia, M. Villen-Guzman, J.M. Rodriguez-Maroto, J.M. Paz-Garcia, Technical analysis of CO_2 capture pathways and technologies, J. Environ. Chem. Eng. 10 (2022) 108470, https://doi.org/10.1016/j.jece.2022.108470.
[4] J.-L. Fan, J. Fu, X. Zhang, K. Li, W. Zhou, K. Hubacek, J. Urpelainen, S. Shen, S. Chang, S. Guo, X. Lu, Co-firing plants with retrofitted carbon capture and storage for power-sector emissions mitigation, Nat. Clim. Chang. 13 (2023) 807–815, https://doi.org/10.1038/s41558-023-01736-y.
[5] C.-Y. Cheng, C.-C. Kuo, M.-W. Yang, Z.-Y. Zhuang, P.-W. Lin, Y.-F. Chen, H.-S. Yang, C.-T. Chou, C.-Y. Cheng, C.-C. Kuo, M.-W. Yang, Z.-Y. Zhuang, P.-W. Lin, Y.-F. Chen, H.-S. Yang, C.-T. Chou, CO_2 capture from flue gas of a coal-fired power plant using three-bed PSA process, Energies 14 (2021), https://doi.org/10.3390/en14123582.
[6] L. Jiang, A. Gonzalez-Diaz, J. Ling-Chin, A.P. Roskilly, A.J. Smallbone, Post-combustion CO_2 capture from a natural gas combined cycle power plant using activated carbon adsorption, Appl. Energy 245 (2019) 1–15, https://doi.org/10.1016/j.apenergy.2019.04.006.
[7] J. Oexmann, A. Kather, Post-combustion CO_2 capture in coal-fired power plants: comparison of integrated chemical absorption processes with piperazine promoted potassium carbonate and MEA, Energy Procedia 1 (2009) 799–806, https://doi.org/10.1016/j.egypro.2009.01.106.
[8] X.Y.D. Soo, J.J.C. Lee, W.-Y. Wu, L. Tao, C. Wang, Q. Zhu, J. Bu, Advancements in CO_2 capture by absorption and adsorption: a comprehensive review, J. CO2 Util. 81 (2024) 102727, https://doi.org/10.1016/j.jcou.2024.102727.
[9] Y. Wu, X. Chen, J. Ma, Y. Wu, D. Liu, J. Mi, W. Xie, System integration for coal-fired power plant with post combustion CO_2 capture: comparative study for different solid dry sorbents, Fuel 280 (2020) 118561, https://doi.org/10.1016/j.fuel.2020.118561.
[10] U. Khan, C.C. Ogbaga, O.-A.O. Abiodun, A.A. Adeleke, P.P. Ikubanni, P.U. Okoye, J.A. Okolie, Assessing absorption-based CO_2 capture: research progress and techno-economic assessment overview, Carbon Capture Sci. Technol. 8 (2023) 100125, https://doi.org/10.1016/j.ccst.2023.100125.
[11] Y. Hu, W. Liu, Y. Yang, M. Qu, H. Li, CO_2 capture by Li_4SiO_4 sorbents and their applications: current developments and new trends, Chem. Eng. J. 359 (2019) 604–625, https://doi.org/10.1016/j.cej.2018.11.128.
[12] R. Han, Y. Wang, S. Xing, C. Pang, Y. Hao, C. Song, Q. Liu, Progress in reducing calcination reaction temperature of calcium-looping CO_2 capture technology: a critical review, Chem. Eng. J. 450 (2022) 137952, https://doi.org/10.1016/j.cej.2022.137952.
[13] R. Chang, X. Wu, O. Cheung, W. Liu, Synthetic solid oxide sorbents for CO_2 capture: state-of-the art and future perspectives, J. Mater. Chem. A 10 (2022) 1682–1705, https://doi.org/10.1039/D1TA07697C.
[14] Y. Hu, R. Fu, W. Liu, D. Yao, S. Yan, Lithium-based ceramics in nonsilicates for CO_2 capture: current status and new trends, J. Mater. Chem. A 10 (2022) 1706–1725, https://doi.org/10.1039/D1TA09629J.
[15] J. Buckingham, T.R. Reina, M.S. Duyar, Recent advances in carbon dioxide capture for process intensification, Carbon Capture Sci. Technol. 2 (2022) 100031, https://doi.org/10.1016/j.ccst.2022.100031.
[16] F. Raganati, F. Miccio, P. Ammendola, Adsorption of carbon dioxide for post-combustion capture: a review, Energy Fuel 35 (2021) 12845–12868, https://doi.org/10.1021/acs.energyfuels.1c01618.
[17] M.T. Dunstan, F. Donat, A.H. Bork, C.P. Grey, C.R. Müller, CO_2 capture at medium to high temperature using solid oxide-based sorbents: fundamental aspects, mechanistic insights, and recent advances, Chem. Rev. 121 (2021) 12681–12745, https://doi.org/10.1021/acs.chemrev.1c00100.
[18] J. Chu, J. Guo, Y. Guo, B. Guo, P. Huang, Z. Zhang, C. Zhao, Solid-state synthesis of alkaline lithium ceramics for integrated CO_2 capture and conversion to syngas, J. Environ. Chem. Eng. 13 (2025) 115105, https://doi.org/10.1016/j.jece.2024.115105.

[19] M.T. Izquierdo, A. Turan, S. Garcia, M. Maroto-Valer, Optimization of Li_4SiO_4 synthesis conditions by solid state method for maximum CO_2 capture at high temperature, J. Mater. Chem. A (2018), https://doi.org/10.1039/C7TA08738A.

[20] E. Stefanelli, M. Puccini, S. Vitolo, M. Seggiani, CO_2 sorption kinetic study and modeling on doped-Li_4SiO_4 under different temperatures and CO_2 partial pressures, Chem. Eng. J. 379 (2020) 122307, https://doi.org/10.1016/j.cej.2019.122307.

[21] Y. Zhang, Y. Gao, H. Pfeiffer, B. Louis, L. Sun, D. O'Hare, Q. Wang, Recent advances in lithium containing ceramic based sorbents for high-temperature CO_2 capture, J. Mater. Chem. A 7 (2019) 7962–8005, https://doi.org/10.1039/C8TA08932A.

[22] R. Fu, W. Gan, H. Yu, J. Yi, Y. Hu, An in-depth investigation on Li_2CuO_2 sorbents for CO_2 capture: from experimental evaluation to DFT study, Chem. Eng. J. 505 (2025) 159832, https://doi.org/10.1016/j.cej.2025.159832.

[23] M.L. Grasso, P. Arneodo Larochette, F.C. Gennari, CO_2 capture properties of Li_4SiO_4 after aging in air at room temperature, J. CO2 Util. 38 (2020) 232–240, https://doi.org/10.1016/j.jcou.2020.02.002.

[24] C. Zhao, L. Wang, L. Huang, N.M. Musyoka, T. Xue, J. Rabeah, Q. Wang, Recent advances in intermediate-temperature CO_2 capture: materials, technologies and applications, J. Energy Chem. 90 (2024) 435–452, https://doi.org/10.1016/j.jechem.2023.11.024.

[25] H.A. Lara-García, E. Vera, J.A. Mendoza-Nieto, J.F. Gómez-García, Y. Duan, H. Pfeiffer, Bifunctional application of lithium ferrites (Li_5FeO_4 and $LiFeO_2$) during carbon monoxide (CO) oxidation and chemisorption processes. A catalytic, thermogravimetric and theoretical analysis, Chem. Eng. J. 327 (2017) 783–791, https://doi.org/10.1016/j.cej.2017.06.135.

[26] E. Bernabé-Pablo, Y. Duan, H. Pfeiffer, Developing new alkaline ceramics as possible CO_2 chemisorbents at high temperatures: the lithium and sodium yttriates ($LiYO_2$ and $NaYO_2$) cases, Chem. Eng. J. 396 (2020) 125277, https://doi.org/10.1016/j.cej.2020.125277.

[27] T. Harada, T. Alan Hatton, Tri-lithium borate (Li_3BO_3); a new highly regenerable high capacity CO_2 adsorbent at intermediate temperature, J. Mater. Chem. A 5 (2017) 22224–22233, https://doi.org/10.1039/C7TA06167F.

[28] C. Villa-Pérez, P. Arneodo Larochette, D.B. Soria, F.C. Gennari, Thermodynamic and kinetic properties of Li_3BO_3 modified by the alkali fluorides addition in the CO_2 capture process, Chem. Eng. J. 450 (2022) 138118, https://doi.org/10.1016/j.cej.2022.138118.

[29] M.D. Morales, P. Arneodo Larochette, N. San Martín, F. Gennari, Thermodynamic and CO_2 sorption investigations on improved Li_3BO_3-based sorbents by NaOH addition, Chem. Eng. J. 497 (2024) 154702, https://doi.org/10.1016/j.cej.2024.154702.

[30] Y. Wang, X. Zhang, B.-I. Min, M. Tanaka, T. Watanabe, Synthesis of amorphous Li_3BO_3 nanoparticles as solid electrolyte for all-solid-state battery by induction thermal plasma, J. Solid State Chem. 318 (2023) 123775, https://doi.org/10.1016/j.jssc.2022.123775.

[31] Z. Tang, J. Choi, J.L. Lorie Lopez, A.C. Co, C.J. Brooks, J.R. Sayre, J.-H. Kim, Optimization of the Li_3BO_3 glass interlayer for garnet-based all-solid-state lithium–metal batteries, ACS Appl. Energy Mater. 5 (2022) 12132–12142, https://doi.org/10.1021/acsaem.2c01606.

[32] M. Xu, J. Lu, Z. Sun, M. Yang, B. Sheng, M. Chen, J. Chen, Q. Zhang, X. Han, Lanthanum doping and surface Li_3BO_3 passivating layer enabling 4.8 V nickel-rich layered oxide cathodes toward high energy lithium-ion batteries, J. Colloid Interface Sci. 673 (2024) 386–394, https://doi.org/10.1016/j.jcis.2024.05.236.

[33] G. Liu, Z. Li, L. Zeng, J. Lin, B. Zheng, H. Liu, L. Chen, F. Wu, Single-crystal Ni-rich layered oxide cathodes with $LiNbO_3$-Li_3BO_3 coating for sulfide all-solid-state batteries, Nano Energy 137 (2025) 110798, https://doi.org/10.1016/j.nanoen.2025.110798.

[34] M.L. Grasso, M.V. Blanco, F. Cova, J.A. González, P.A. Larochette, F.C. Gennari, Evaluation of the formation and carbon dioxide capture by Li_4SiO_4 using in situ synchrotron powder X-ray diffraction studies, Phys. Chem. Chem. Phys. 20 (2018) 26570–26579, https://doi.org/10.1039/C8CP03611J.

[35] M.V. Blanco, K. Kohopää, I. Snigireva, F. Cova, Low temperature solid state synthesis of Li_5FeO_4 and CO_2 capture mechanism via real time in situ synchrotron X-ray diffraction, Chem. Eng. J. 354 (2018) 370–377, https://doi.org/10.1016/j.cej.2018.08.017.

[36] F. Cova, G. Amica, K. Kohopää, M.V. Blanco, Time-resolved synchrotron powder X-ray diffraction studies on the synthesis of Li_8SiO_6 and its reaction with CO_2, Inorg. Chem. 58 (2019) 1040–1047, https://doi.org/10.1021/acs.inorgchem.8b01297.

[37] M.V. Blanco, P.M. Abdala, F. Gennari, F. Cova, Dynamics of phase transitions in Na_2TiO_3 and its possible utilization as a CO_2 sorbent: a critical analysis, React. Chem. Eng. 6 (2021) 1974–1982, https://doi.org/10.1039/D1RE00125F.

[38] F.H. Cova, M.V. Blanco, Tracking sodium cobaltate formation pathways and its CO_2 capture dynamics in real time with synchrotron X-ray diffraction, react, Chem. Eng. 9 (2024) 439–447, https://doi.org/10.1039/D3RE00459G.

[39] J.M. Valverde, S. Medina, Limestone calcination under calcium-looping conditions for CO_2 capture and thermochemical energy storage in the presence of H_2O: an in situ XRD analysis, Phys. Chem. Chem. Phys. 19 (2017) 7587–7596, https://doi.org/10.1039/C7CP00260B.

[40] A. Biasin, C.U. Segre, G. Salviulo, F. Zorzi, M. Strumendo, Investigation of CaO–CO_2 reaction kinetics by in-situ XRD using synchrotron radiation, Chem. Eng. Sci. 127 (2015) 13–24, https://doi.org/10.1016/j.ces.2014.12.058.

[41] A.V. Llewellyn, A. Matruglio, D.J.L. Brett, R. Jervis, P.R. Shearing, A.V. Llewellyn, A. Matruglio, D.J.L. Brett, R. Jervis, P.R. Shearing, Using in-situ laboratory and synchrotron-based X-ray diffraction for lithium-ion batteries characterization: a review on recent developments, Condensed Matter 5 (2020), https://doi.org/10.3390/condmat5040075.

[42] K.T. Møller, B.R.S. Hansen, A.-C. Dippel, J.-E. Jørgensen, T.R. Jensen, Characterization of gas-solid reactions using in situ powder X-ray diffraction, Z. Für Anorg. Allg. Chem. 640 (2014) 3029–3043, https://doi.org/10.1002/zaac.201400262.

[43] P. Alonso Sánchez, K. Thangaian, O.A. Øie, A. Gaarud, M. Rodríguez Gomez, V. Diadkin, J. Campo, F.H. Cova, M.V. Blanco, Toward the controlled synthesis of nanostructured Si and SiO_x anodes for Li-ion batteries via SiO_2 magnesiothermic reduction reaction, ACS Appl. Energy Mater. 8 (2025) 2249–2259, https://doi.org/10.1021/acsaem.4c02836.

[44] K.P. Marshall, H. Emerich, C.J. McMonagle, C.A. Fuller, V. Dyadkin, D. Chernyshov, W. van Beek, A new high temperature, high heating rate, low axial gradient capillary heater, J. Synchrotron Radiat. 30 (2023) 267–272, https://doi.org/10.1107/S1600577522009845.

[45] P. Alonso, M.V. Blanco, F. Cova, M.L. Grasso, M.J. Orozco, Unveiling the Reaction Dynamics of Li_3BO_3 High-capacity CO_2 Sorbent, 2027, https://doi.org/10.15151/ESRF-ES-1699365002.

[46] C. Prescher, V.B. Prakapenka, DIOPTAS: a program for reduction of two-dimensional X-ray diffraction data and data exploration, High Press. Res. 35 (2015) 223–230, https://doi.org/10.1080/08957959.2015.1059835.

[47] J. Rodriguez-Carvajal, Recent advances in magnetic structure determination by neutron powder diffraction, Phys. B Condens. Matter 192 (1993) 55–69, https://doi.org/10.1016/0921-4526(93)90108-I.

[48] O. Arcelus, J. Rodríguez-Carvajal, N.A. Katcho, M. Reynaud, A.P. Black, D. Chatzogiannakis, C. Frontera, J. Serrano-Sevillano, M. Ismail, J. Carrasco, F. Fauth, M.R. Palacin, M. Casas-Cabanas, FullProfAPP: a graphical user interface for the streamlined automation of powder diffraction data analysis, J. Appl. Cryst. 57 (2024) 1676–1690, https://doi.org/10.1107/S1600576724006885.

[49] M. Eom, S. Choi, S. Son, L. Choi, C. Park, D. Shin, Enhancement of lithium ion conductivity by doping Li_3BO_3 in Li_2S-P_2S_5 glass-ceramics electrolytes for all-solid-state batteries, J. Power Sources 331 (2016) 26–31, https://doi.org/10.1016/j.jpowsour.2016.09.032.

[50] S. Ohta, S. Komagata, J. Seki, T. Saeki, S. Morishita, T. Asaoka, All-solid-state lithium ion battery using garnet-type oxide and Li_3BO_3 solid electrolytes fabricated by screen-printing, J. Power Sources 238 (2013) 53–56, https://doi.org/10.1016/j.jpowsour.2013.02.073.

[51] D. Gogoi, N. Kalita, R. Thakuria, Mechanical milling for scaled up manufacturing of nanoparticles, in: N.M. Adassooriya, A. Manipura, A. Husen (Eds.), Ind. Scale Prod. Nanoparticles, Springer Nature, Singapore, 2025, pp. 55–66, https://doi.org/10.1007/978-981-96-9176-0_4.

[52] S. Arfelis, A.I. Martín-Perales, R. Nguyen, A. Pérez, I. Cherubin, C. Len, I. Malpartida, A. Bala, P. Fullana-i-Palmer, Linking mechanochemistry with the green chemistry principles: review article, Heliyon 10 (2024), https://doi.org/10.1016/j.heliyon.2024.e34655.

[53] R. Zhang, X. Shen, Y. Liang, H. Hua, G. Li, F. Yan, Z. Quan, Z. Zhang, A comprehensive investigation of mechanical mixing-thermal activation for CaO-based adsorbent with coal fly ash as a stabilizer, Chem. Eng. J. 522 (2025) 167824, https://doi.org/10.1016/j.cej.2025.167824.

[54] W. Cui, L. Li, Y. Guo, S. Zhang, T. Deng, Heat capacity and thermodynamic property of lithium pentaborate pentahydrate, J. Chem. 2018 (2018) 7962739, https://doi.org/10.1155/2018/7962739.

[55] B.S.R. Sastry, F.A. Hummel, Studies in lithium oxide systems: V, Li_2O-B_2O_3, J. Am. Ceram. Soc. 42 (1959) 216–218, https://doi.org/10.1111/j.1151-2916.1959.tb15456.x.

[56] G. Rousse, B. Baptiste, G. Lelong, Crystal structures of $Li_6B_4O_9$ and $Li_3B_{11}O_{18}$ and application of the dimensional reduction formalism to lithium borates, Inorg. Chem. 53 (2014) 6034–6041, https://doi.org/10.1021/ic500331u.

[57] M.B.I. Chowdhury, M.R. Quddus, H.I. deLasa, CO_2 capture with a novel solid fluidizable sorbent: thermodynamics and temperature programmed carbonation–decarbonation, Chem. Eng. J. 232 (2013) 139–148, https://doi.org/10.1016/j.cej.2013.07.044.

[58] E. Stefanelli, F. Francalanci, S. Vitolo, S. De Santis, M. Puccini, High-temperature CO_2 capture by doped Li_4SiO_4 sorbents: scaling up adsorption and regeneration in a fixed bed reactor, J. Environ. Chem. Eng. 13 (2025) 116102, https://doi.org/10.1016/j.jece.2025.116102.

[59] X. Yan, Y. Li, X. Ma, J. Zhao, Z. Wang, Performance of Li_4SiO_4 material for CO_2 capture: a review, Int. J. Mol. Sci. 20 (2019) 928, https://doi.org/10.3390/ijms20040928.

[60] S. Chen, C. Qin, W. Yuan, D.P. Hanak, J. Ran, Kinetic study and modeling on the regeneration of Li_4SiO_4-based sorbents for high-temperature CO_2 capture, Fuel Process. Technol. 222 (2021) 106976, https://doi.org/10.1016/j.fuproc.2021.106976.

[61] K. Wang, F. Gu, P.T. Clough, Y. Zhao, P. Zhao, E.J. Anthony, Molten shell-activated, high-performance, un-doped Li_4SiO_4 for high-temperature CO_2 capture at low CO_2 concentrations, Chem. Eng. J. 408 (2021) 127353, https://doi.org/10.1016/j.cej.2020.127353.

[62] K. Nagao, A. Hayashi, M. Tatsumisago, Mechanochemical synthesis and crystallization of Li_3BO_3–Li_2CO_3 glass electrolytes, J. Cerma. Soc. Jpn. 124 (2016) 915–919, https://doi.org/10.2109/jcersj2.16114.

[63] R.D. Shannon, B.E. Taylor, A.D. English, T. Berzins, New Li solid electrolytes, Electrochim. Acta 22 (1977) 783–796, https://doi.org/10.1016/0013-4686(77)80035-2.

[64] T. Okumura, T. Takeuchi, H. Kobayashi, All-solid-state lithium-ion battery using $Li_{2.2}C_{0.8}B_{0.2}O_3$ electrolyte, Solid State Ion. 288 (2016) 248–252, https://doi.org/10.1016/j.ssi.2016.01.045.

[65] X.-Y. Feng, C.-H. Wang, H. Pan, Z. Ji, X.-M. Wang, L. Fang, F. Luo, Interstitial Li^+ and Li^+ migrations in the $Li_{2+x}C_{1-x}B_xO_3$ solid electrolyte, J. Phys. Chem. C 126 (2022) 18466–18474, https://doi.org/10.1021/acs.jpcc.2c05189.

[66] Y. Yang, J. Cao, Y. Hu, J. Sun, S. Yao, Q. Li, Z. Li, S. Zhou, W. Liu, Eutectic doped Li_4SiO_4 adsorbents using the optimal dopants for highly efficient CO_2 removal, J. Mater. Chem. A 9 (2021) 14309–14318, https://doi.org/10.1039/D1TA01404H.

[67] R. Xiong, J. Ida, Y.S. Lin, Kinetics of carbon dioxide sorption on potassium-doped lithium zirconate, Chem. Eng. Sci. 58 (2003) 4377–4385, https://doi.org/10.1016/S0009-2509(03)00319-1.

[68] J.F. Stebbins, Z. Xu, D. Vollath, Cation exchange rates and mobility in aluminum-doped lithium orthosilicate: high-resolution lithium-6 NMR results, Solid State Ion. 78 (1995) L1–L8, https://doi.org/10.1016/0167-2738(95)00122-M.